

SOURCE ANALYSIS OF DAYTIME MSTID USING OBSERVATION AND SIMULATION

JONAH, O. F. ^{1,2}, E. A. KHERANI ², E. R. DE PAULA²

¹SRI International, Geospace
333 Ravenswood Ave, Menlo Park, CA 94025
²National Institute for Space Research (INPE)
São José Dos Campos, São Paulo, Brasil.

E-mail: olusjonah@gmail.com

Abstract

Atmospheric gravity waves are known to be the source of medium-scale traveling ionospheric disturbances (MSTIDs) in the upper atmosphere. In recent studies, these gravity waves have mostly been linked to weather convection activities from tropospheric altitudes during the daytime. In this research work, we study the generation and dynamics of daytime MSTIDs induced by tropospheric convections over the Brazilian sector. Both observational and theoretical tools are employed to pursue these objectives. Data from space and ground-based instruments such as a network of GNSS receivers, digisonde, and meteorological satellites (GOES Satellite) are analyzed to identify the driving source of AGW-MSTIDs. The convectional-Atmosphere-Ionosphere-Coupled model (CAI-CM) is adapted to incorporate the dynamics of convectively generated AGWs and their coupling to the ionosphere. The model is used to analyze the source of AGW as they propagate from the lower atmosphere to the upper atmosphere and how MSTIDs are dependent on the sources that generate them.

Keywords: MSTIDs, Atmospheric Gravity waves, GNSS, Tropospheric convection

1.0 Introduction

Medium scale travelling ionospheric disturbances (MSTIDs) are signature of density perturbation in the upper atmosphere caused by gravity waves travelling in natural atmosphere (Hunsunker, 1982). MSTIDs observations using Global Navigation Satellite System (GNSS) have also been studied in recent years (e.g. Tsugawa et al. 2004, 2007, Otsuka et al., 2004, 2013, Jonah et al., 2016, 2017 and 2018 etc.). Tsugawa et al. (2007) using the GPS-TEC methodology, showed Total Electron Content (TEC) maps for the daytime between 19:20 UT (13:20CST) and 22:00 UT (16:00 CST) on November 28, 2006 over North America where daytime MSTIDs propagate southeastward around mid-day and southwestward in the late afternoon at a velocity of 100 - 200 m/s, with a wavelength of 300 - 1000 km and a peak-to-peak amplitude larger than ~ 0.5 TEC. Nighttime MSTIDs were also investigated. Following the same methodology above, Otsuka et al, (2013) analyzed the TEC data obtained with the GPS observables over Europe and investigated the time sequence of two-dimensional TEC perturbation during daytime. The TEC perturbation can be seen to have a phase front aligned in the east-west direction and propagate in the equatorward direction, which is in agreement with the Tsugawa et al. (2007). More recently, Jonah et al., (2018) revealed that Large scale and equatorward propagating TIDs are generated from constant energy input from the auroral source as a result of geomagnetic storm while Medium scale poleward propagating TIDs are seeded by gravity waves from convection activity. They also pointed out that TID activity in the ionosphere can be significant in the transfer of energy and momentum from one region to another. Furthermore, studies of MSTIDs using Incoherent/Coherent Scatter Radar and All-Sky Cameras have also reported consistent prediction of Perkins (1973) linear theory. For example, Fukao et al. (1991) investigated the coherent backscatter of 50 MHz radar waves from the mid-latitude F region by using the Japanese MU radar. When the radar was tilted 57.8° toward due north in fixed beam mode, they observed that intense and turbulent echoes usually were from irregular patches moving upward and away from the radar at Doppler speeds of 100-200 m/s. When the radar was in multiple beam mode, irregular patches were observed to move from east to west at velocities around 150 m/s. Further, many RTI (range-time-intensity) plots showed a downward slant which indicated a northwest movement of patches. Kelley and Fukao (1991) compared some instability mechanisms and regarded that Perkins instability was the best one to explain the

above coherent radar observations. Kelley (2011) showed five examples of mid-latitude airglow features which were compared with airglow from the magnetic equator. The striking difference is that the mid-latitude features are not aligned with the magnetic meridian and do not move eastward as the equatorward features do, but rather propagate southwestward in the northern hemisphere and northwestward in the southern hemisphere which is in line with the Perkins (1973) theory. Behnke (1979) observed banded structures of raised and lowered F region layer in the ionosphere on five out of eight nights over Arecibo under solar minimum conditions. The structures were aligned along the northwest-southeast direction and propagated to the southwest with a height difference of the order of 50 km and phase velocities usually between 13 and 61 m/s.

AGW properties are similar to that of TID described above. Therefore, TIDs are just manifestations of AGW in the ionosphere. Waves created by convection are as numerous (i.e. with many different scales) as the generation mechanisms (different convective structures or other mechanisms). Convectively-induced waves can, for example, be triggered by the bulk release of latent heat (Piani et al., 2000), the obstacle effect produced by the convective column on the stratified shear flow above (Pfister et al., 1993), or the mechanical pump effect due to vertical oscillations of updrafts and downdrafts behaving as an oscillating rigid body (Alexander and Barnett, 2007). All three seeding can be coupled, depending strongly upon the local shear and the vertical profile and time dependence of the latent heating (Fritts and Alexander, 2003). Atmospheric general circulation modeling studies (Medvedev et al., 2011; Yigit et al., 2012) and numerical simulations (Vadas and Fritts, 2006) have demonstrated that convectively generated gravity waves can propagate from the lower atmosphere into the thermosphere-ionosphere system. Their wave momenta and energies are deposited at background atmosphere (Horinouchi et al., 2002), which has been supposed to be crucial in various aspects of the dynamic and thermal structure of the middle atmosphere. They are not just characterized by a single prominent frequency as in the case for topographic generated waves, instead have wide spectra (e.g. internal gravity waves). The connection between generation of gravity waves and active convection regions has been studied by many authors (e.g., Fritts et al., 2009, Vadas et al., 2009). Deep clouds near the tropopause region are indicative of regions of active convection and a likely source of gravity waves (Vadas et al., 2009, Jonah et al. 2016 and 2018). Cold brightness temperature suggests deep convective

plumes and convective overshoot which are a convenient launching platform for gravity waves (Fritts et al., 2009, Vadas et al., 2009). Shume et al. (2014) also show evidence of deep tropospheric convection induces AGW in the behavior of electrojet and E region electric field.

In the present study, we identify and compare case studies of AGW-induced TIDs during convective and non-convective storm periods to understand the effect of tropospheric convection-induced AGW on TIDs. In the second part, CAI-CM is used as a coupling model to simulate convective-induced AGW between the troposphere and the ionosphere. Two numerical experiments were carried out (1) by using a strong convective forcing and (2) by using a weak convective forcing. The convective forcing induced AGW from the tropospheric level propagates to the thermospheric level and reproduces the observed TIDs with convectional forcing/strong convection forcing and non-convectional forcing/weak convection forcing. In section 2 we present the method of MSTID and convection activity determination. Section 3 is about the observational results. Section 4 introduced the CAI_CM as a coupling model to simulate convective-induced AGW between the troposphere and ionosphere and presents two numerical experiments: (1) by using a strong convective forcing and (2) by using a weak convective forcing. Section 5 presents the summary and conclusion.

2.0 Method of MSTID determination

Two-dimensional maps of absolute vertical TEC are derived with time resolution of 10 minutes and spatial resolution of $0.5^\circ \times 0.5^\circ$ in latitude and longitude. We focus on the *TEC* measurements during 12-17 UT (9 – 14LT) thus boundary condition effects are avoided. From this TEC map, keograms are generated by choosing a cut along latitude and a cut along longitude directions. These keograms consist of the temporal variation of TEC distributed along the latitude and longitude. A polynomial fit with order 7 is employed to each of these spatially distributed time series and corresponding best fits are obtained. From this, the MSTIDs are derived by subtracting the TEC best fit (*polyfit*) from the TEC mean. More specific details on the MSTID determination are discussed by Jonah et al. (2016).

2.1 Determination of convectonal and non-convectonal activity days

According to Vadas et al. (2009) deep clouds near the tropopause region are indicative of regions of active convection and a likely source of gravity waves. Cold brightness temperature suggests deep convective plumes and convective overshoot which are convenient launching platforms for gravity waves (Fritts et al., 2009). Gravity waves generated from the convective sources can propagate into the higher altitude and penetrate deep into the upper atmosphere (Yigit et al., 2008; Fritts et al., 2009). Hence, we used the water vapor and infrared temperature data obtained from the Brazilian CPTEC/INPE web site to demonstrate the tropospheric convection activity. A strong convection activity implies that the difference in water vapor and infrared is greater than 0°C (i.e. $\text{WV} - \text{IR} > 0^{\circ}\text{C}$) while a low convection activity implies that the difference between the water vapor and the infrared temperature is less than 0°C (i.e. $\text{WV} - \text{IR} < 0^{\circ}\text{C}$) (Shume et al., 2014). The analysis is carried out for December summer month of 2011 which represent moderate solar activity. The prominently strong convection activities and the GNSS data availability contributes to our choice for the study of this time period.

3.0 MSTIDS OBSERVATION RESULTS

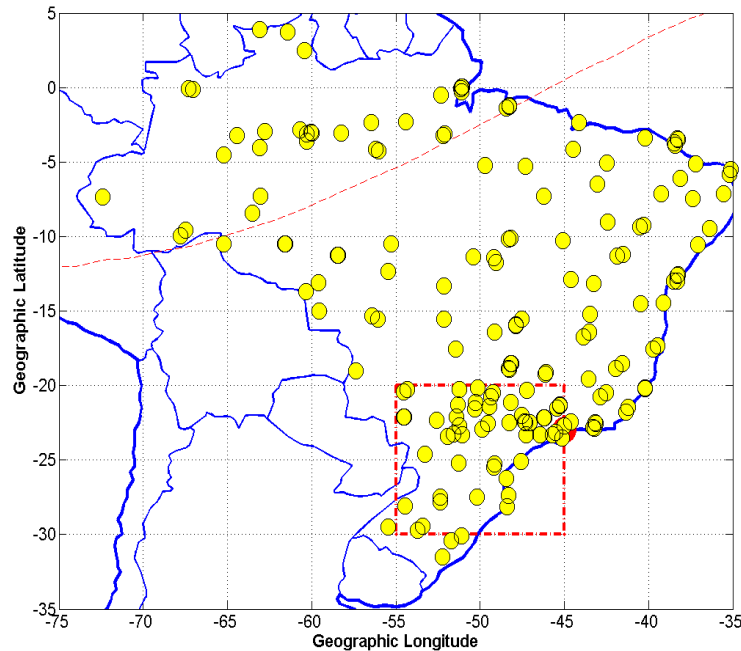


Figure 1 - The yellow circles in the red dash box show the distribution of the GPS receivers used, the red circle shows the station of the digisonde location and the red-dash line shows the magnetic equator (Jonah et al, 2016).

Figure 1(square box) represents the area of focus and where better distribution of GPS receivers is located. There are up to 40 GPS receivers in the $10^\circ \times 10^\circ$ square box.

Figures 2 present MSTID derived from GNSS-TEC measurements during quiet geomagnetic conditions ($k_p \leq 3$) on 5, December 2011 during 12-17 UT.

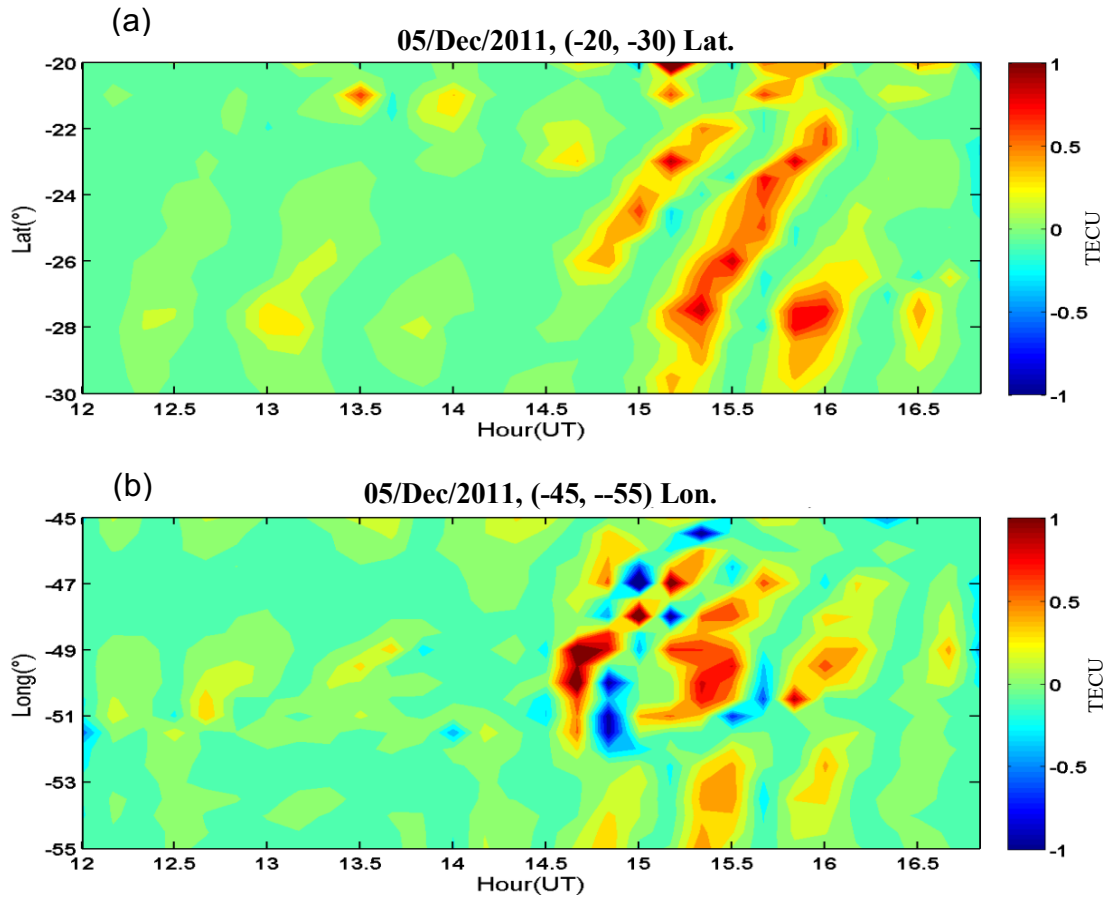


Figure 2 (a) and (b) represent MSTID propagation in latitude and longitude respectively as a function of universal time (Jonah et al. 2016).

From Figures 2(a) and with reference to Jonah et al. (2016), it is possible to observe the phase of the oscillation shifts in time while moving towards equator and eastward which maximize around 13-16 UT. The peaks are observed to mostly shift towards equatorward/eastward in time, this behavior is more dominant and last longer in latitude than in longitude. The MSTIDs travel with a range of 155-189 m/s and with a wavelength range of 255-389 Km in the southward to northward direction, while in the westward to eastward direction these values are 122-142 m/s and 184-322 km. The wave generally travels with higher velocity and larger wavelength in southward to northward direction than in westward to eastward direction (i.e. MSTID travels faster equatorward). The wave periodicity ranges between 30 - 55 minutes and maximum amplitude around 13-16 UT with ~ 1 TECU. These properties are similar to past literatures (e.g. Hernández-Pajares et al., 2006; 2012; Tsugawa et. al., 2007, Otsuka et al., 2004; Jonah et al., 2016; 2017; 2018).

3.1 Tropospheric weather convection source

According to Jonah et al. (2016 and 2018) convective forcing from the tropospheric region would induce vertical propagating gravity wave which if survive to the thermospheric region could leads to the generation of MSTID on arrival in the ionosphere. Figure 3. (courtesy Jonah et al., 2016) shows the AGW-MSTIDs based on their comparison with strong and weak tropospheric weather convection activity on two different days. For easy comprehensive discussion, we refer 5 and 7 December 2011 as D5 and D7.

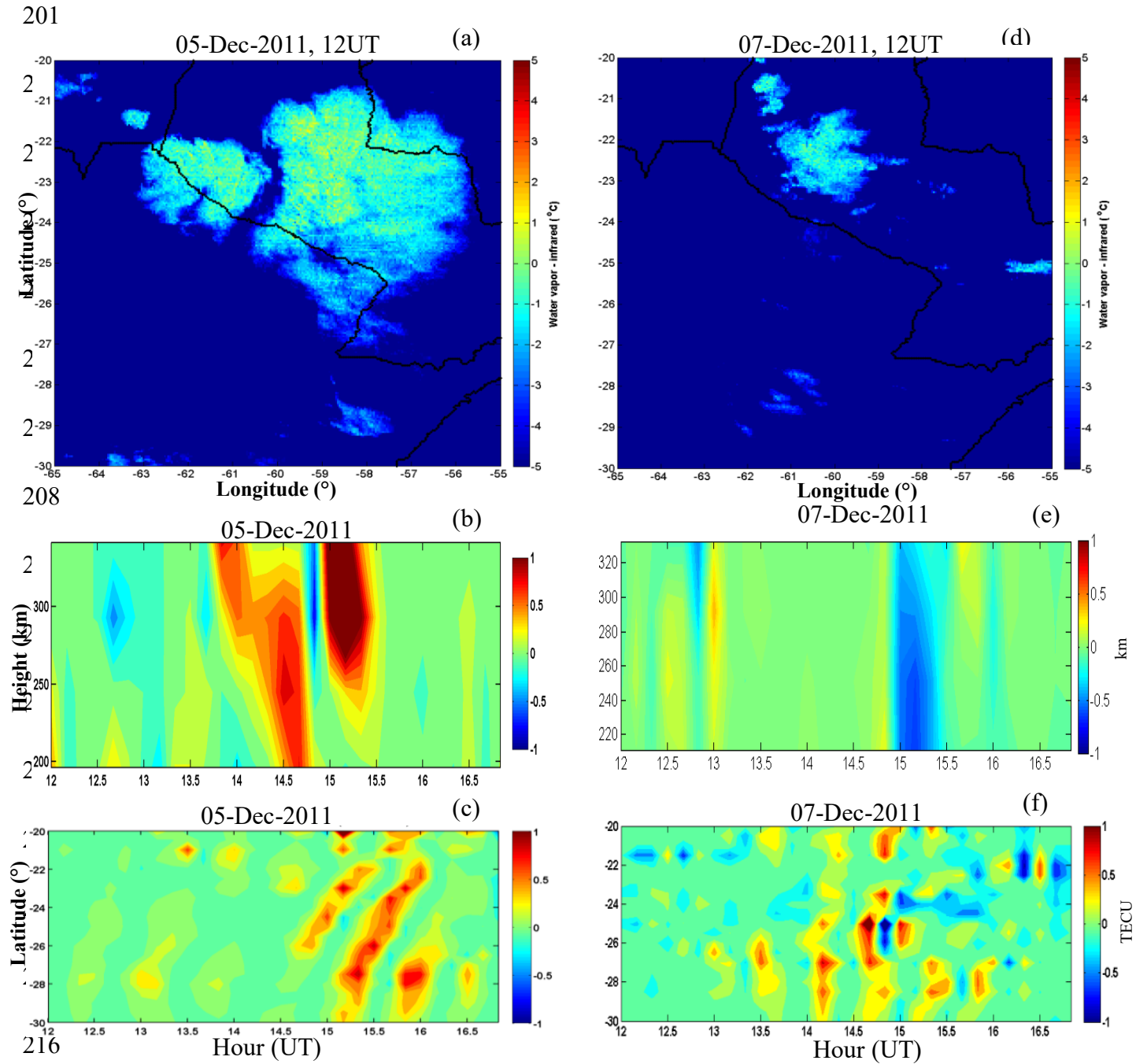


Figure 3 - Comparison of the observed strong convective storm on D5 and the weak convective storm on D7 with their respective cross-correlation of Δh and ΔTEC (Jonah et al. 2016).

222

223 Panel (a) represents an example of strong convection activity. Panel (b) represents the
224 signature of gravity wave activity as presented by variation in the true height, Panel (c) is the
225 strong and well-defined MSTIDs on a strong weather convection day. On the other hand,
226 Panel (d) represents an example of weak convection activity. Panel (e) shows the signature
227 of gravity wave activity presented by variation in the true height. Panel (e) represents weak
228 and not well-defined MSTIDs obtained on a weak convection activity day. The deep and
229 weak convection activities are seen very close to the site of the AGW and MSTIDs
230 observation. By comparing Figure 3a to 3c, it is possible to clearly observe that the AGW
231 and the MSTIDs activities on a strong convection day are much well defined than on a weak
232 convection day represented by Figures 3d to 3f. This suggests clear evidence of strong
233 convection activity as an important factor of AGW seeding and consequent MSTIDs activity.
234 It is also possible to note that the cloud distribution locations are correlated with the observed
235 propagation direction of the MSTIDs particularly that of the eastward directions.

236

237

4.0 MSTID SIMULATION RESULTS

In order to understand the generating mechanism of AGW-MSTIDs represented in section 3, we present a unified approach where coupling of acoustic-gravity wave (AcGWs) and associated dynamics of the polarization electric field are considered. First, we give brief theoretical and physical descriptions of the model. Then, two numerical experiments were carried out (1) by using a strong convective forcing and (2) by using a weak convective forcing.

According to Kherani et al. (2016), it is possible to obtain AGW wind perturbations using a derived hydrodynamic wave equation of AGW from the Navier-Stokes equations through taking the derivative of the momentum equation for wind and substituting the time density, wind perturbation and pressure from the Stokes equation. The ambient atmosphere conditions are obtained from SAMI2 model (Huba et al., 2000). The Earth's magnetic field is obtained by using IGRF. By taking the time derivative of the momentum equation for the wind, and again substituting time derivatives of the density (ρ), wind perturbation (\vec{W}') and pressure (p) from the Navier-Stokes equations, the wave equation for the wind perturbation \vec{W}' of AGW is obtained in the following form (Kherani et al., 2012):

According to Kherani et al. (2016) the derived hydrodynamic wave equation of AGW from the Navier Stoke equations by taking the derivative of the momentum equation for wind and substituting the time density (ρ), wind perturbation and pressure (p) from the Stoke equation, they obtained the wind perturbation \vec{W}' of AGW as follows:

$$\frac{\partial^2 \vec{W}'}{\partial t^2} = \frac{1}{\rho} (\gamma p \nabla \cdot \vec{W}') - \frac{\nabla p}{\rho^2} \nabla \cdot (\rho \vec{W}') + \frac{1}{\rho} \nabla (\vec{W}' \cdot \nabla) p + \frac{\partial}{\partial t} \left(\left[\eta \nabla^2 \vec{W}' + \left(\zeta' + \frac{\nu}{3} \right) \nabla (\nabla \cdot \vec{W}') \right] \right) - \frac{\partial}{\partial t} (\vec{W}' \cdot \nabla \vec{W}') \quad (1)$$

$$\vec{W}' = \vec{W} + \vec{W}_b$$

$$\frac{\partial \rho}{\partial t} + \nabla \cdot (\rho \vec{W}') = 0 \quad (2)$$

$$\frac{\partial p}{\partial t} + (\vec{W}' \cdot \nabla) p + \gamma p \nabla \cdot \vec{W}' = 0 \quad (3)$$

Where η is the dynamic viscosity coefficient, \vec{W}' is the perturbation wind, $p = R\rho T$ is the pressure, ρ, T are the atmospheric mass density and temperature. From the right hand side of equation (1), the first term corresponds to the acoustic wave, second and third terms correspond to the gravity wave, the fourth term with the dynamic viscosity coefficient η corresponds to the viscous dynamics and last term corresponds to the inertial force. ς represents the ratio of second viscosity coefficient to kinematic viscosity coefficient.

4.1 Coupling the atmospheric and ionospheric

The ionospheric simulation is performed using set of hydromagnetic equations given below. The detailed explanations for the equations are given by Kherani et al. (2016) and Huba et al. (2000).

$$\frac{\partial \vec{u}_s}{\partial t} = \frac{q_s}{m_s} (\vec{E} + \vec{u}_s \times \vec{B}_o) - \nu_s \vec{u}_s + \nu_s \vec{W}', \quad (4)$$

$$\frac{\partial n_s}{\partial t} + \nabla \cdot (n_s \vec{u}_s) = P - L, \quad (5)$$

$$\nabla^2 \vec{E} - \nabla (\nabla \cdot \vec{E}) = \frac{1}{c^2} \frac{\partial^2 \vec{E}}{\partial t^2} = 0, \quad (6)$$

$$\vec{J} = \tilde{\sigma} \cdot \vec{E} + \vec{J}_w; \quad \vec{J}_w = e(n_i \vec{u}_i^w - n_e \vec{u}_e^w), \quad (7)$$

Where (n_s, \vec{u}_s) are, respectively, the number density and velocity of plasma fluid 's' is the ions (i), electrons (e), ($q_{i,e} = Z_{i,e} - e$), \vec{B}_o is the Earth's magnetic field and \vec{J}_w is the ionospheric current density caused by the AGWs, (\vec{E}, \vec{J}) in above equations are the electric field and net ionospheric current, ν_s is the frequency of collision between species s to neutral,

$\tilde{\sigma}$ is the ionospheric conductivity tensor and $c = \frac{1}{\sqrt{\mu_o \epsilon_o}}$. P and L are the production and loss of ions and electrons by photoionization and chemical reactions. The production term 'P' in (5) is derived from SAMI2 model. The chemical loss term, 'L', in equation (5) is

retained through effective recombination rate as taken by Kherani et al (2016). In addition to wave equation (6), \vec{E} also satisfies the charge neutrality condition given by the following equation (Kherani et al., 2012).

$$\nabla \cdot \vec{J} = 0 \text{ or } \nabla \cdot (\tilde{\sigma} \cdot \vec{E} + \vec{J}_w) = 0 \Rightarrow \nabla \cdot \vec{E} = -\tilde{\sigma}^{-1} (\nabla \tilde{\sigma} \cdot \vec{E} + \nabla \cdot \vec{J}_w) \quad (8)$$

At $t = 0$, ambient atmosphere and ionosphere (P_o, ρ_o, n_o, v_o, T) are obtained from SAMI2 model (Huba et al., 2000). Equations (1 to 8) are solved numerically using finite-difference method in three dimension simulation domain in spherical polar coordinate that consists of altitude (r), latitude (θ) and longitude (ϕ). The implicit Crank-Nicholson scheme is employed to perform the time integration leading to a matrix equation that is subsequently solved by the Successive-Over-Relaxation method. The magnetic dipole coordinate system (p, q, ϕ) is adopted where p, q, ϕ represent the coordinates outward normal to the Earth's magnetic field, northward directed parallel to the Earth's magnetic field and azimuth angle (positive towards west) respectively. The north-south and east-west boundaries of simulation domain are 45°S -5°S and $75^\circ-35^\circ\text{W}$ which covers the region of interest. The lower boundary for the atmosphere and ionosphere are chosen to be the 10 km and 160 km respectively. The upper boundary is chosen to be 600 km for both the atmosphere and ionosphere.

The flow chart (Figure 4) for the Convection Atmospheric-Ionospheric Coupling Model is shown below. The Atmospheric part of the model is first initiated using the hydrodynamic equations as given in equations 1 to 3. In the presence of convective forcing at tropospheric height a primary gravity wave is generated which propagates upward. With the given dissipation terms, a secondary gravity is excited around 120 to 250 km altitude. Then the coupling of atmosphere with ionosphere is conducted next using equation (4) and by solving the hydromagnetic equations (5) to (8) the electric field is calculated to give a divergent free current. Finally, the MSTIDs are generated as TEC perturbation and the code is updated again for the next time.

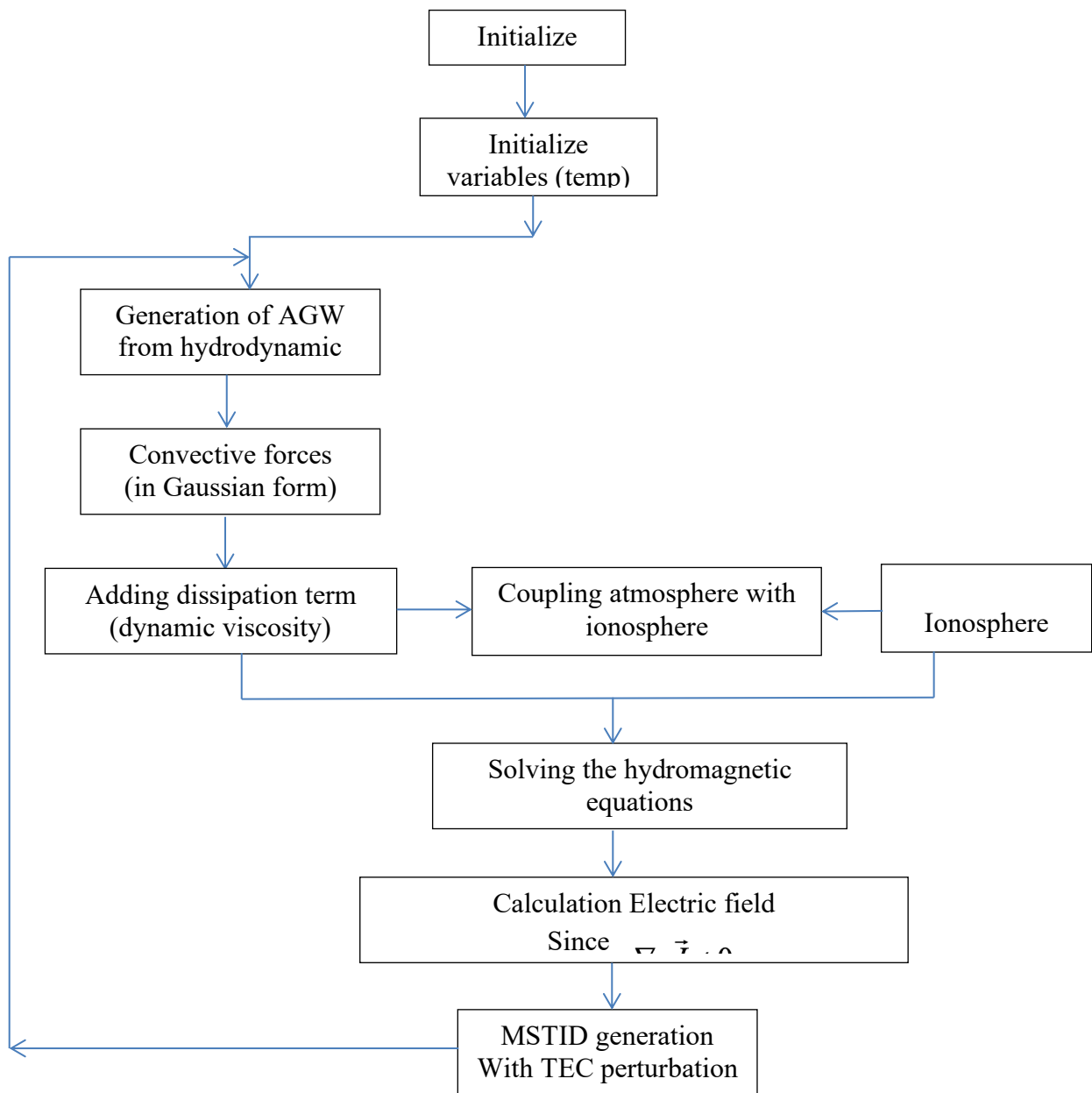


Figure 4 - Dynamic flow chart of the Convection Atmosphere-Ionosphere Coupling Model

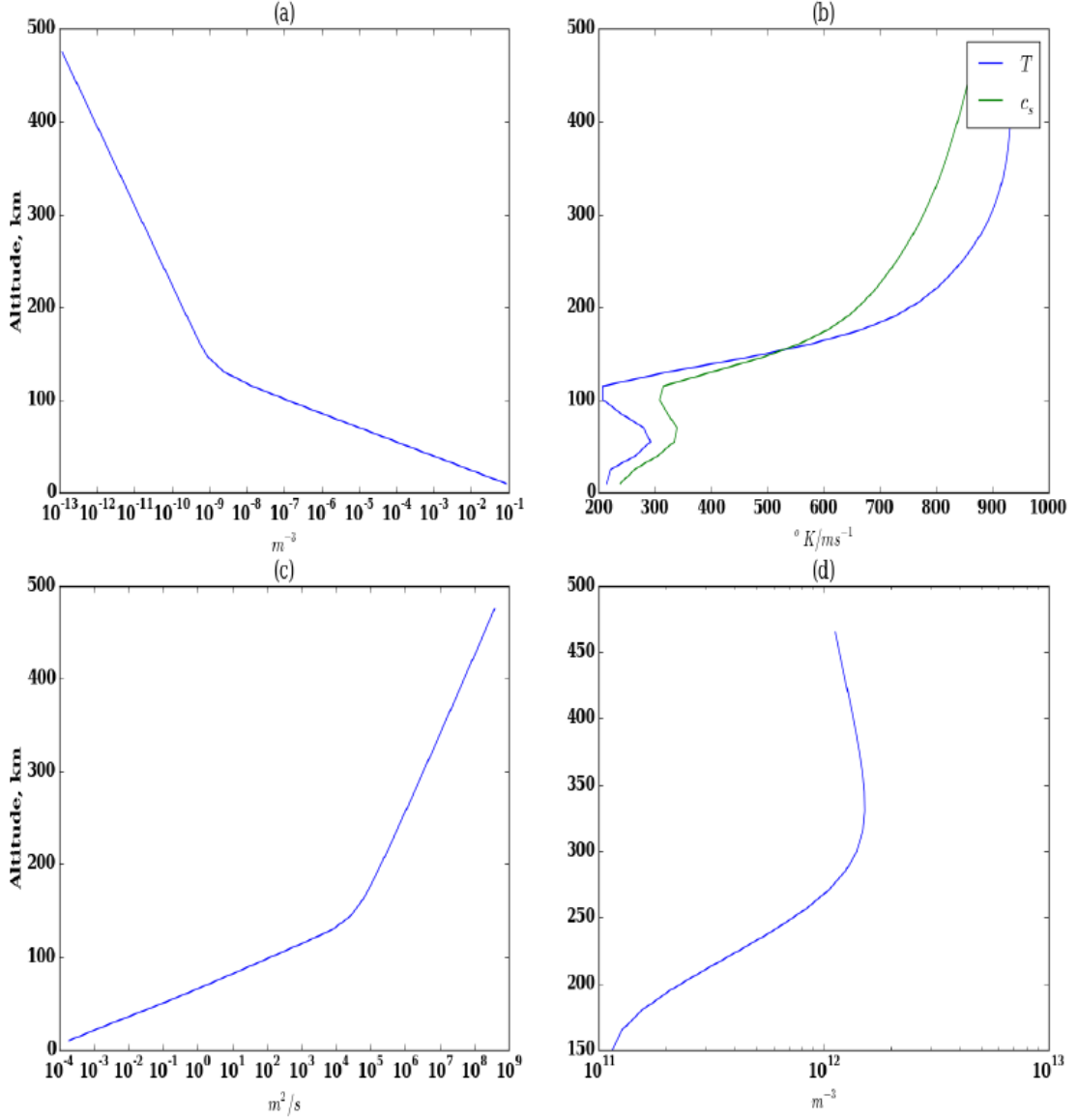


Figure 5 - Ambient atmospheric and ionospheric conditions: (a-d) Altitude profiles of Atmospheric density (ρ_o), Temperature/Sound speed (T_o / c_s), Dynamic viscosity ($\eta = \mu / \rho_o$) and Ionospheric density (n_o). To the first order, atmosphere and ionosphere are considered to be horizontally stratified at the simulation beginning time $t = 0$.

In Figure 5, from (a) to (d), the atmospheric mass density (ρ), acoustic speed ($\sqrt{\gamma p / \rho}$) kinematic viscosity (η) and ionospheric number density (n_o) are shown. The ambient electric field is considered to be zero.

In order to understand the MSTIDs dynamics and mechanism observed and presented in the section 3 and in Jonah et al. (2016), we focus on comparative study of MSTIDs observed on 05 (D1) and 07 (D2) December 2011 as represented by Figures 3(a) and 3(d). These two days represent the extreme conditions of convective and MSTIDs dynamics. For example, on D1 (D2) the convective activity is strong (weak), manifested by large (small) convective cloud. The MSTIDs observed on these two days reveal positive correlation with the convective activity such that on D1 (D2), they have distinct (not so obvious) propagation characteristics on keograms.

The convective forcing is considered to be of Gaussian form as follows (Zettergren and Snively, 2015):

$$W_r = (r = 0, \theta, \varphi, t) \equiv W_F = 10^{-3} e^{-(t-t_0)^2 / \infty_t^2} e^{-(\theta-\theta_0)^2 / \infty_\theta^2} e^{-(\varphi-\varphi_0)^2 / \infty_\varphi^2} m/s, \quad (9)$$

where $t_0 = 4000$ seconds, $\theta_0 = -22.5^\circ$, $\varphi_0 = -57.5^\circ$ are the coordinates of maxima of W_r and $\infty_t, \infty_\theta, \infty_\varphi$ are the half-maximum-full-width of Gaussians in respective coordinates. In the present study, $\infty_t = 2000$ seconds is considered, based on common convective forcing characteristics. Based on $\infty_\theta = \infty_\varphi$, two case studies, D1 and D2, are classified. In D1 (D2), ∞_θ is considered to be 2° (1°) respectively. In Figure 6, 3D view of the convective forcing is shown for D1. We may note that the effective size of convective forcing is $\sim 10^\circ$ which is noted in observation on 05 December 2011 as presented in Figures 3a. Accordingly, for D2, the size is $\sim 5^\circ$ as also consistent with the observation on 07 December 2011. We refer simulation exercises of D1 and D2 as numerical experiment NE1 and NE2.

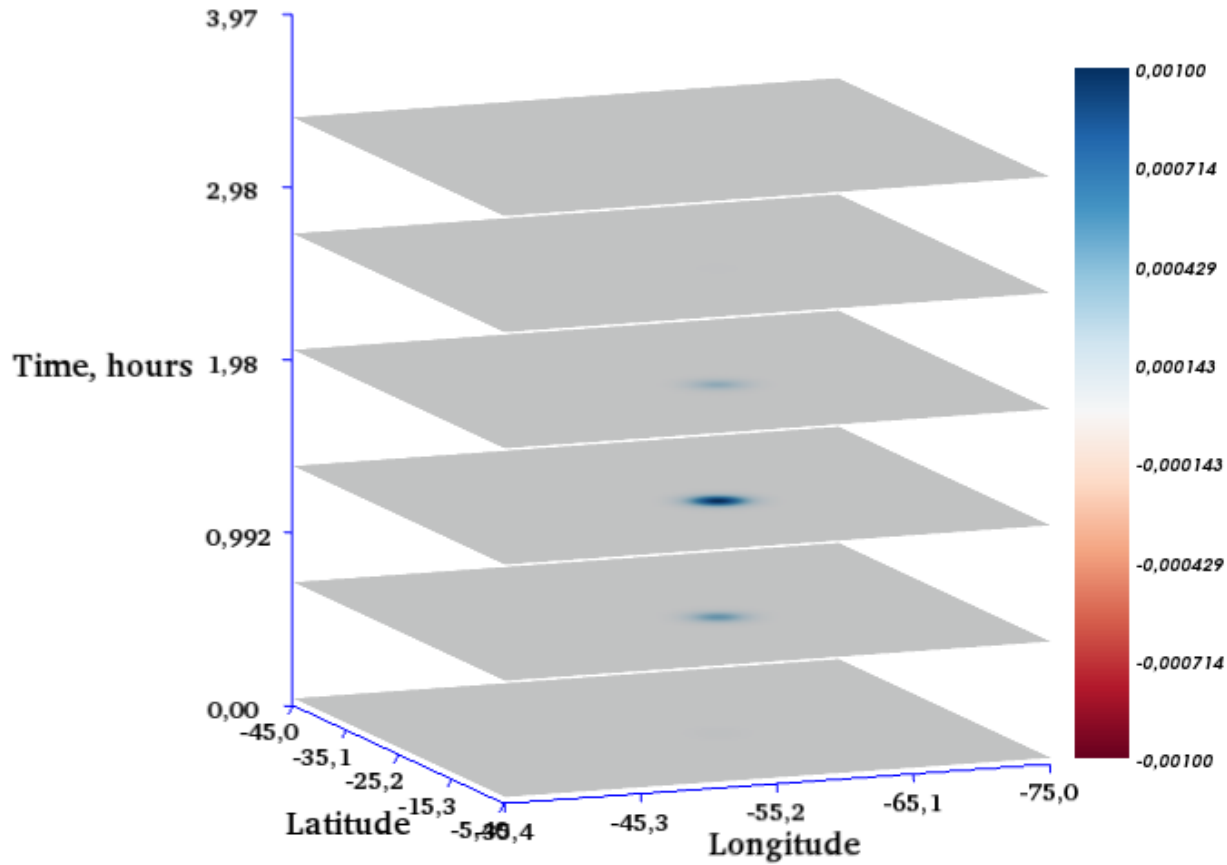


Figure 6 - Convective Forcing characteristics: 3D view demonstrates the forcing, in the form of uplift i.e., W_r at the lower boundary of simulation volume which is at 10 km height. It is of Gaussian type in time (t), longitude (φ) and latitude (θ). The color bar unit is in m/s.

At the lower boundary i.e., at 10 km altitude, the outward normal component W_r of the wind \vec{W} is continuous and equals to W_F for all time. The lower boundary condition $W_r = W_F$ at all time acts as the driving source for the excitation of AGWs. At the subsequent time, other wind components W_θ , W_φ in entire simulation domain and W_r in entire simulation domain except at the lower boundary are self-consistently determined from the equation (1). The presence of AGWs modifies the atmosphere and ionosphere which in turn alters the characteristics of AGWs itself. This cause-effect mechanism continues for next 3 hours which is the time chosen to stop the simulation.

4.3 Simulation results (Numerical Experiment 1)

Recall that our first and second simulation exercises as mentioned earlier are D1 and D2 and are referred to as numerical experiment 1 and 2 (i.e. NE1 and NE2). In Figures 7 – 8, we present the simulation results of AGWs for D1. In Figure 7, the three dimensional distribution of vertical wind amplitude (W_r) of AGWs at few selected times are shown. In Figure 8, snapshots of the horizontal distribution of W_r at the altitude of 200 km altitude is shown.

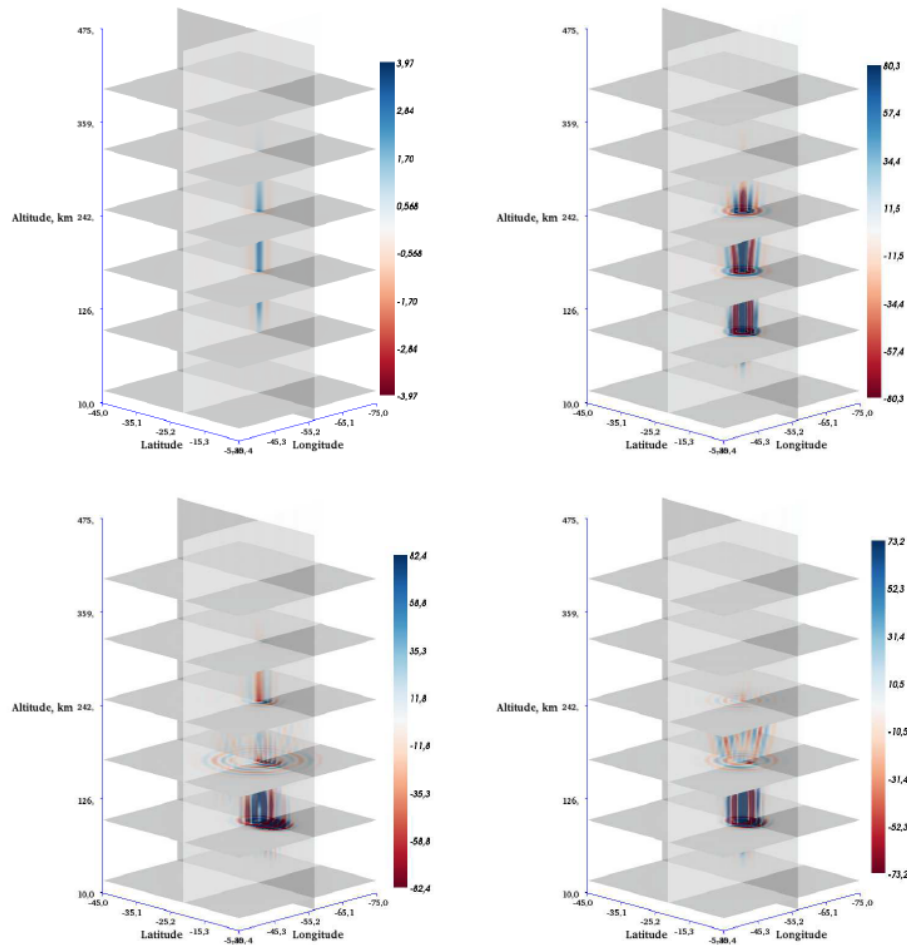


Figure 7 - AGW simulation: 3D volume snapshots of amplitude (W_r) of AGWs at four selected times $t=2000, 4000, 6000, 8000$ seconds organized in clockwise direction.

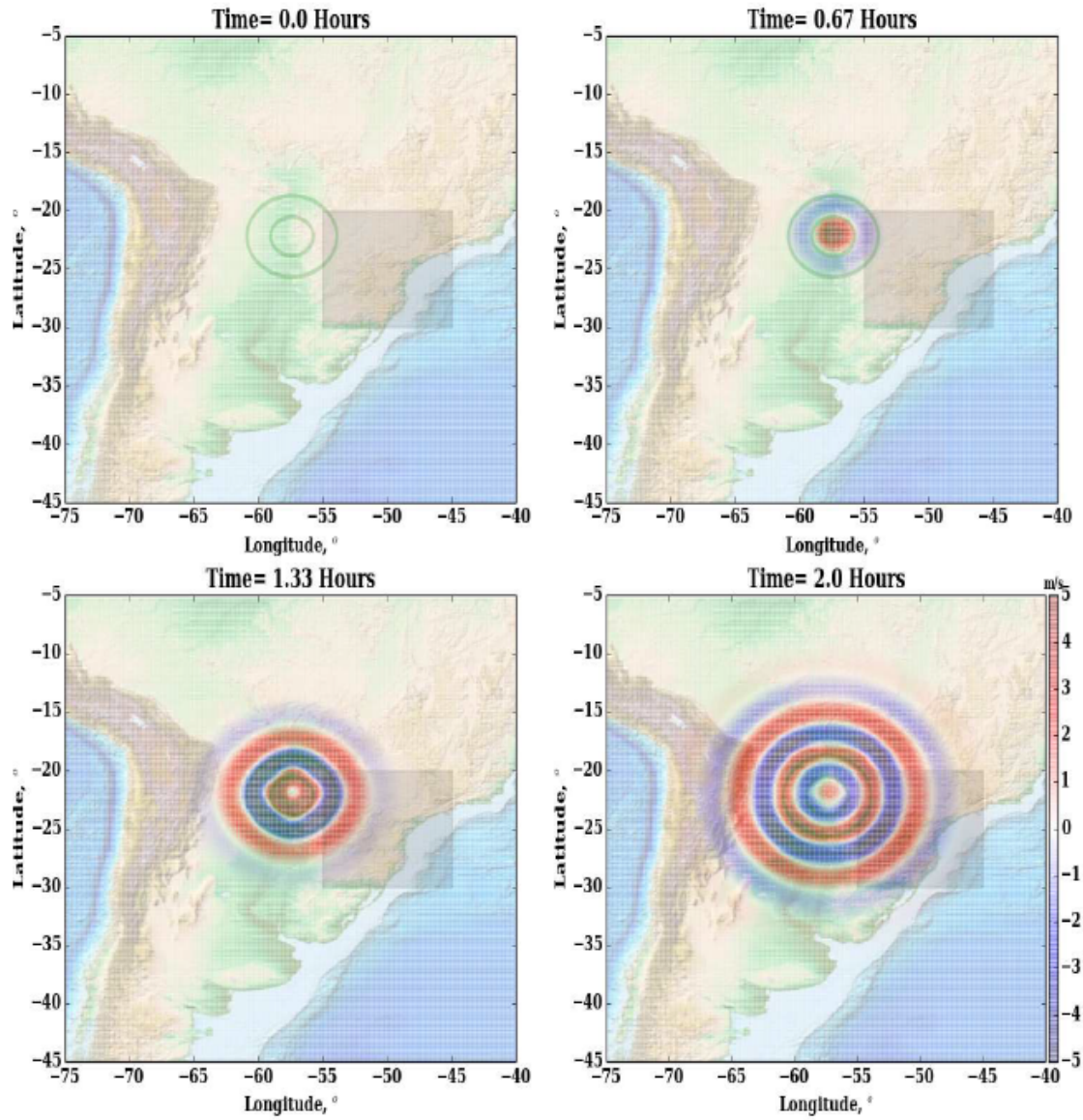


Figure 8 - AGW simulation: 2D horizontal snapshots of amplitude (W_r) of AGWs at four selected times $t = 2000, 4000, 6000, 8000$ seconds and at altitude of 200 km altitude. The green contours represent the convective forcing at 10 km altitude. The shaded rectangle represents the GNSS receiver locations used in the observations.

We note in Figure 7 – 8 that the forcing at 10 km altitude that is, the disturbance introduced at 10 km altitude propagates in space and time such that its amplitude and horizontal coverage increases with altitude up to 300 km and then decreases. This is because in the thermosphere, the horizontal coverage is much wider ($\sim 30^\circ$) than the forcing size ($\sim 10^\circ$) itself which is a result of viscous dissipation and secondary generation of AGWs in the thermosphere. This process that generates the secondary AGWs is referred as the thermospheric body force as discussed in the Vadas et al. (2009) and Jonah et al. (2016). The horizontal propagation is accomplished in the form of concentric circular wavefronts with wavelength of $\sim 3^\circ - 5^\circ$, as noted in Figure 8 that progressively propagate outward from the convective forcing.

In Figure 9, the simulation results for ΔTEC is presented. Where $\Delta\text{TEC} = \text{TEC}(t) - \text{TEC}_{\text{amb}}(t)$ where $(\text{TEC}(t)$ and $\text{TEC}_{\text{amb}}(t))$ are derived from ionospheric density by solving the continuity equation with and without including AGWs. The simulated TEC is obtained by integrating the density along the path perpendicular to the field lines.

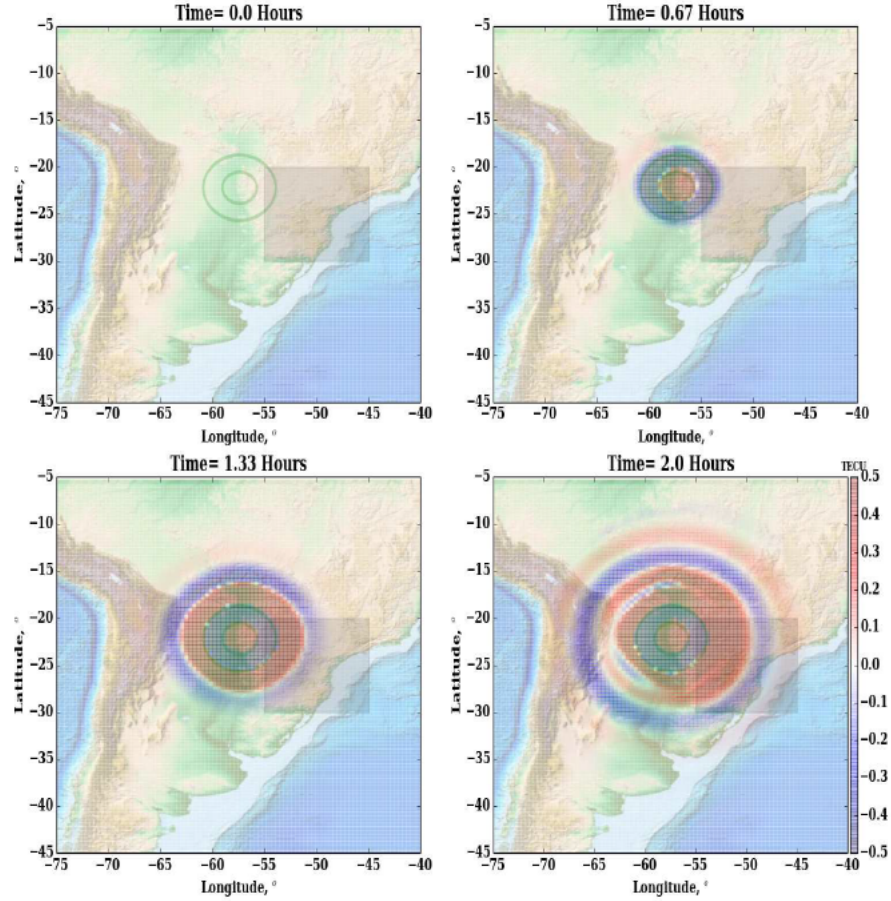


Figure 9 - TEC simulation: 2D snapshots of ΔTEC at four selected times $t=2000, 4000, 6000, 8000$ seconds.

In this figure, it is possible to observe snapshots of ΔTEC distribution in form of radial propagation. Interestingly, TEC disturbance in Figure 9 also reveals similar evolution and propagation characteristics as the AGWs in Figure 8. We may note that W_r of ~ 50 m/s and ΔTEC of ~ 0.5 TECU is excited, as a result of convective forcing of $\sim 10^{-3}$ m/s. In Figure 10, latitude and longitude keograms of W_r and ΔTEC just as observed in the experimental study of section 3 are presented.

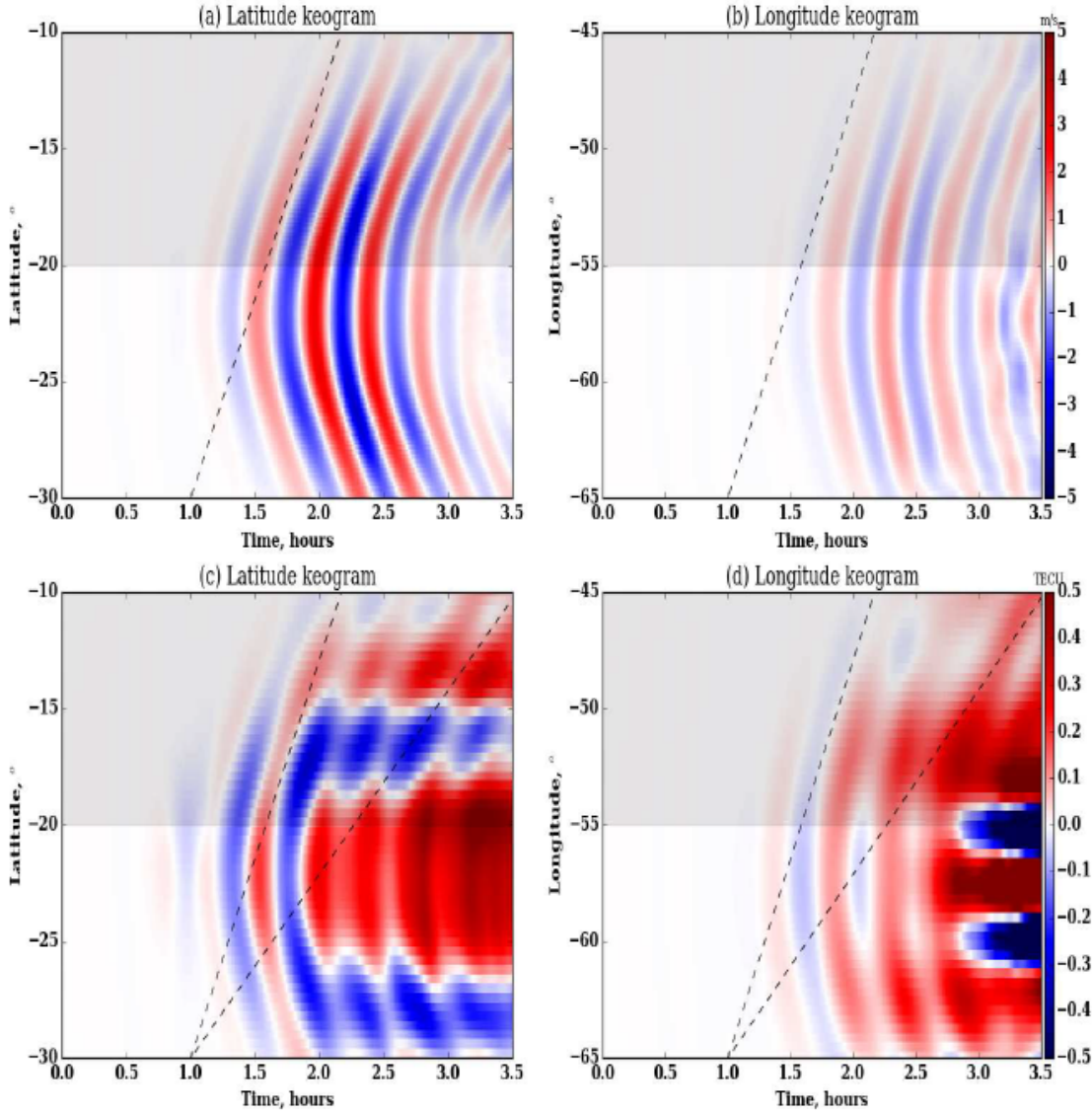


Figure 10 - Keograms: Latitude keograms at fixed longitude ($\varphi = -50.4^\circ$) and longitude keograms at fixed latitude ($\theta = -12.4^\circ$) for W_r in the upper panel and for ΔTEC in the lower panel. The dashed lines represent the slopes of 650 m/s and 300 m/s.

The keogram in Figure 10 reveals the equatorward-eastward propagation of ΔTEC , similar to the observed propagation of MSTIDs in the previous section. We also note the period of wavefront to be ~ 30 minutes which is another aspect similar to the observed results. Both wavelength of $\sim 3^\circ - 6^\circ$ and period of ~ 30 minutes classify the simulated TEC disturbances as MSTIDs. In Figure 10, it is also possible to clearly identify the acoustic wavefront

propagating horizontally with ~ 650 m/s as evident from the dashed line which has its slope equals to 650 m/s. In addition, we also identify the slower propagating gravity wavefront after 2.5 hours and their propagation speed is ~ 250 m/s. Our observation results are likely to miss the acoustic wavefront owing to the slower sampling rate >30 seconds. For this reason, the observed keogram reveals only the gravity wavefronts.

Another important difference we note between observed and simulated latitude keograms is the difference in the location of equatorward propagating wavefront. In contrast to their apparent observed location between $-25^\circ - -20^\circ$, the simulated location covers between $-20^\circ - -15^\circ$. It should be noted that the observed keogram is plotted with respect to the receiver location. However, the observed ΔTEC corresponds to the IPP locations which may be significantly different from the receiver location. In the present case, these IPPs seem to cover the northward of the area covered by the receiver and therefore in this case, the observed and simulated locations may not differ considerably. The differences noted between observed and simulated ΔTEC may be caused by various reasons, notable among them are the differences in the ambient conditions, convective forcing and the procedure of estimating ΔTEC

4.4 Simulation results (Numerical Experiment 2)

The simulation results for NE2 are presented in Figures 11 – 13 in same format as Figures 8 – 10 respectively. We note the excitation of AGWs and subsequent development of ΔTEC disturbances in the form of concentric circular wavefronts, similar to NE1. However, in NE2, the wavefronts are weak and the horizontal coverage is limited in comparison to NE1. This difference arises from the weak convective forcing in NE2 that launches shorter horizontal wavelengths.

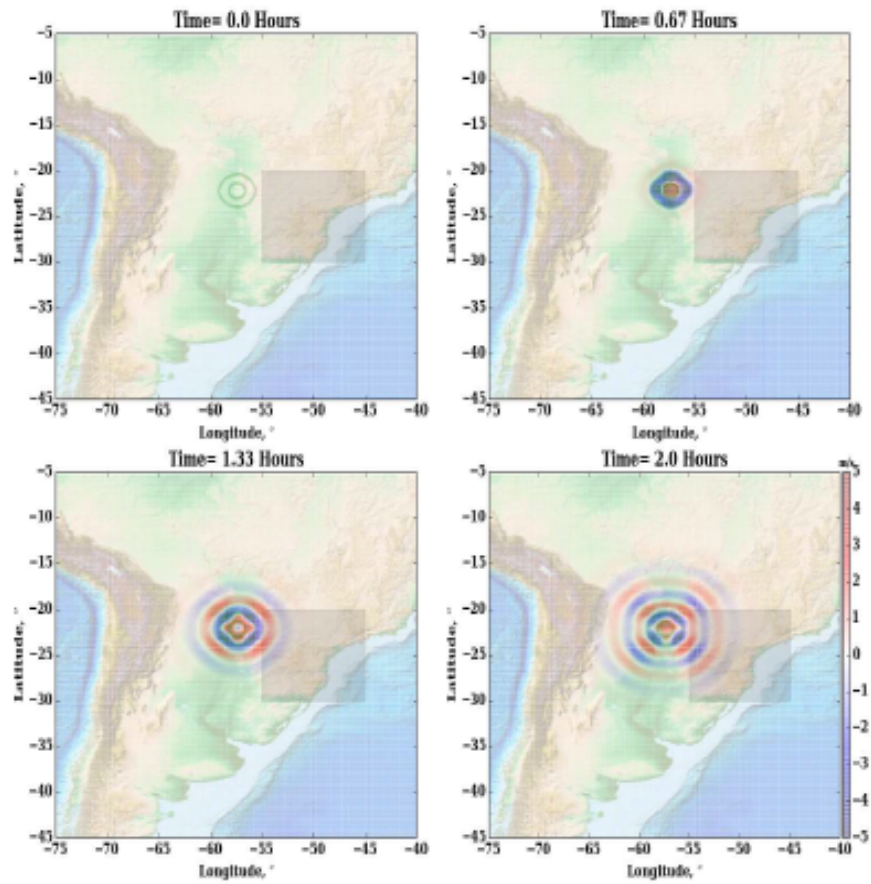


Figure 11 - NE2: same format as Figure 8.

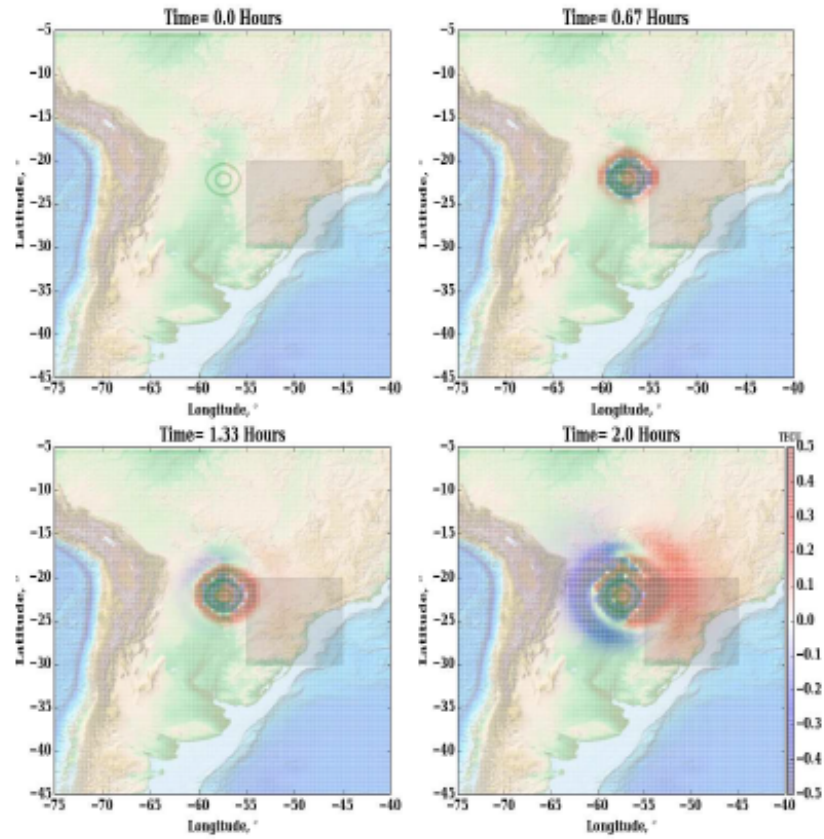


Figure 12 - NE2: same format as Figure 9

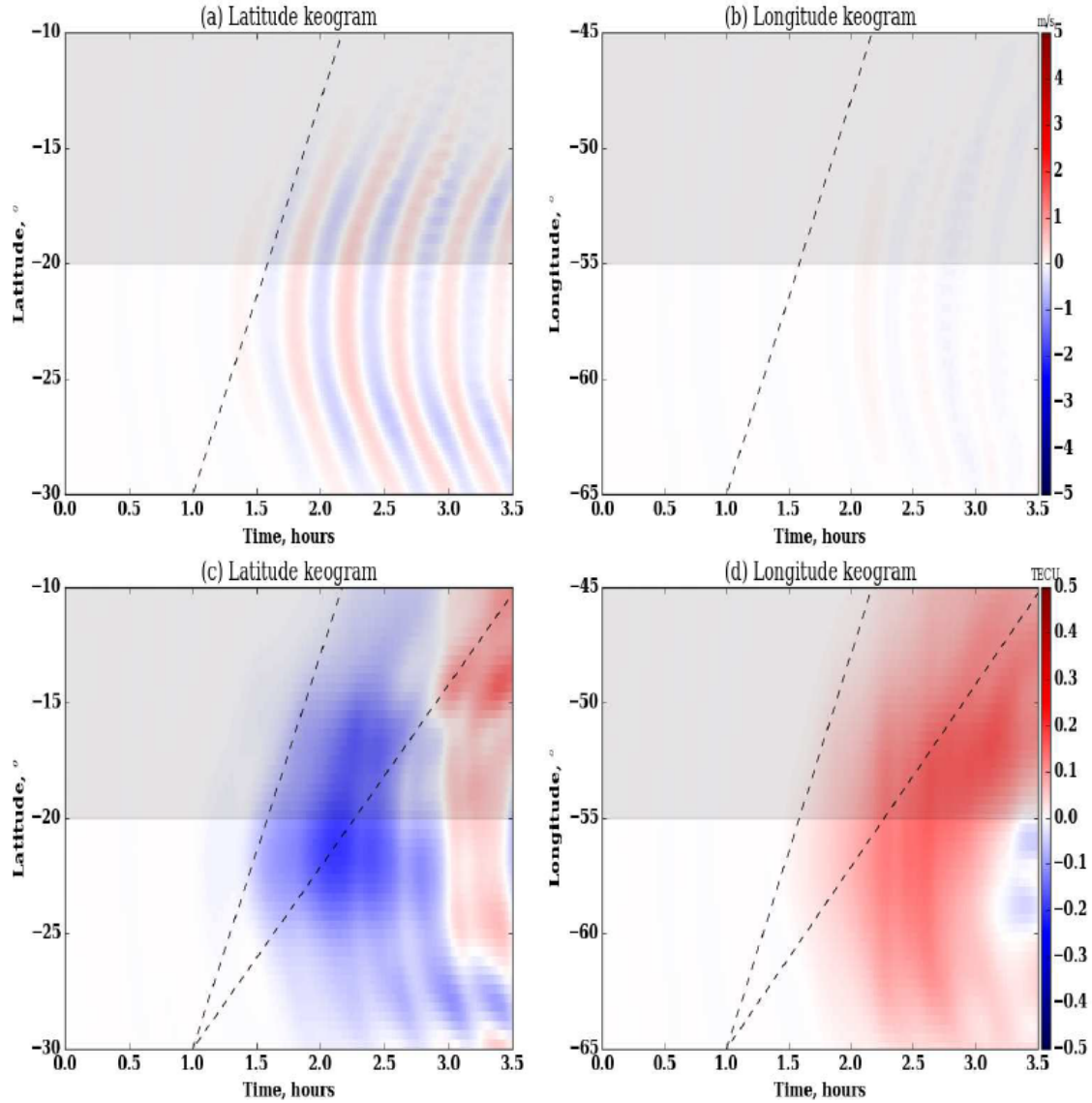


Figure 13 - NE2: same format as Figure 10

As mentioned earlier the simulated MSTIDs are located more towards equator than in the observation results. This difference is possibly due to the fact that IPPs of the observations are located more towards equator. At the same time, it is possible to bring these MSTIDs within the similar latitude region as the observation by relocating the convective forcing to more towards southward. The keograms and the circular propagation from this numerical experiment which we refer as NE1_2 are shown in Figure 14 and Figure 15 in which the convective forcing is located in 30°S – 25°S, in contrast to its location in 25°S – 20°S in NE1. We note that the MSTIDs are now located in similar region as the observation.

Therefore, for future research, it could be recommended to use the IPP position of TEC observations rather than using the receiver positions.

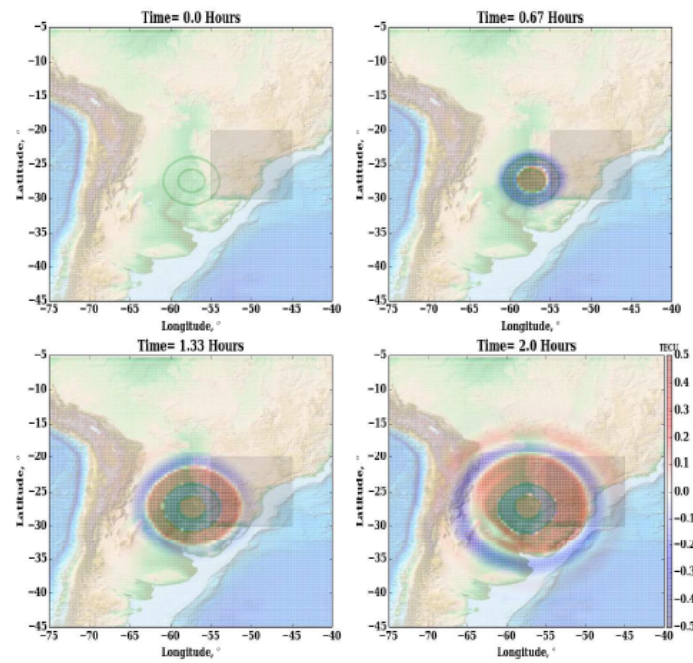


Figure 14. NE1_2 results: In same format as Figure 9.

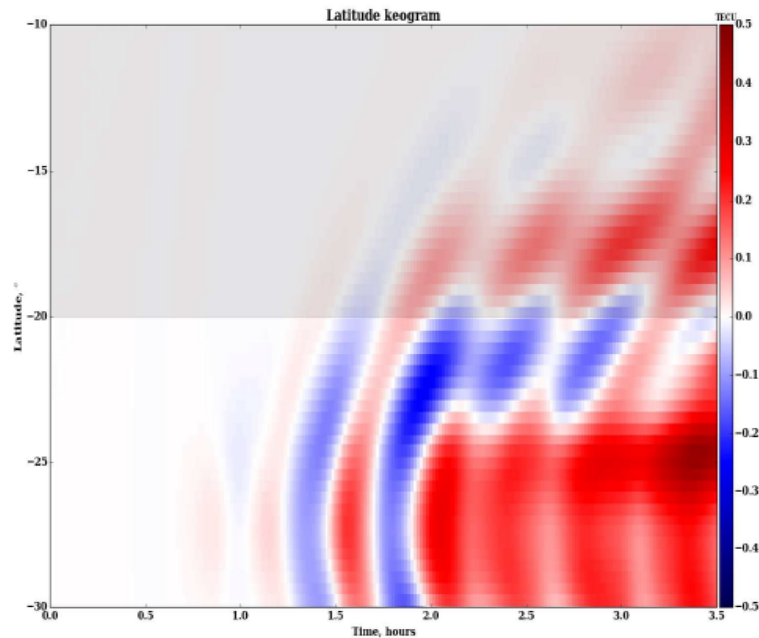


Figure 15. NE1_2 results: In same format as Figure 13.

The table below shows the similarities and good agreement of the observation results with the CAI-CM simulation results. For example, both simulation and observation show the same direction of propagation (which is the northeastward propagation in the south hemisphere) and the observation results for parameters such as wavelength, period and velocity are found to be within the domain of the simulated results for the same parameter. Though the simulation recorded higher velocity than the observation, this different could result from the AcGW source of the simulation rather than the AGW source of the observation.

Table 1. The characteristics differences between the observed and the simulated MSTIDs.

| Properties | Observed MSTIDs | Simulated MSTIDs |
|------------------|--------------------|--------------------|
| Wavelength | 255 - 480 km | 300 - 600 km |
| Period | 20 - 55 min | ≤ 30 min |
| Velocity | 122 - 260 m/s | 250 - 600 m/s |
| Direction | Northeastward - SH | Northeastward - SH |
| Geomag. activity | Quiet | Quiet |

5.0 CONCLUSIONS

This study provided insights to the understanding of the mechanism responsible for MSTIDs generations and propagations using both observational and simulation techniques over the low latitude regions of the Brazilian sector. Most importantly it shows that MSTIDs are not restricted to mid-latitudes but are also abundant in low latitude regions. Two 3-dimensional ionospheric models, the Convective Atmosphere-ionosphere coupling model (CAI-CM) were also used to give perceptions and interpretations of the mechanisms responsible for the observed MSTIDs.

We showed that the observed MSTIDs are caused by tropospheric weather activity and use atmospheric and ionospheric coupling model to analyzed the source of convective forcing induced AGW as they propagate from the lower atmosphere to the upper atmosphere and how MSTIDs are generated and dependent on the sources that generate them. Our results show a close correlation between enhanced MSTIDs and AGW during daytime on day-to-day basis and bring out the issue about the convection activity as AGW generation. We also show that eastward propagation directions of MSTIDs are due mainly to the distributions of the source around the observation sites. The simulation results from the model are mostly in good agreement with the observation result of this study. Our model (CAI-CM) prove how different convective sources (strong/weak) excite different level of MSTIDs (well-developed/weakly developed MSTIDs).

Acknowledgements

Jonah O.F. and E.R. de Paula would like to acknowledge the supports from Conselho Nacional de Desenvolvimento Científico e Tecnológico (CNPq) under process 133429/2011-3 and 202531/2019-0 grants respectively. E.A. Kherani is grateful to FAPESP under process 2011/21903-3. The authors also acknowledge Dra. Inez Batista for the Digisonde data.

References

- ALEXANDER ,M. J; BARNET, C. Using satellite observations to constrain parameterizations of gravity wave effects for global models, **Journal of Atmospheric Science**, v. 64(5), p. 1652–1665, 2007.
- BEHNKE, R. A. F. Layer height bands in the nocturnal ionosphere over Arecibo, **Journal of Geophysical Research**, v. 84, p. 974-978, 1979.
- FRITTS, D. C; WANG, L; WERNE, J; LUND, T; AND WAN, K., Gravity wave instability dynamics at high Reynolds numbers. Part I: wave field evolution at large amplitudes and high frequencies, *J. Atmos. Sci.*, 66, 1126 - 1148, doi:10.1175/2008JAS2726.1, 2009.
- FRITTS, D. C. AND ALEXANDER, M. J. Gravity wave dynamics and effects in the middle atmosphere, **Rev. Geophys.**, v. 41(1), p. 1003, doi:10.1029/2001RG000106, 2003.
- FUKAO, S.; KELLEY, M. C; SHIRAKAWA, T; TAKAMI, T; YAMAMOTO, M; TSUDA, T; KATO, S. Turbulent upwelling of the midlatitude ionosphere, 1, Observational results by the MU radar, **Journal of Geophysical Research**, v. 96, p. 3725-3746,1991.
- HERNANDEZ-PAJARES, M; JUAN, J. M; SANZ, J. Medium-scale traveling ionospheric disturbances affecting GPS measurements: Spatial and temporal analysis, **Journal of Geophysical Research**, v. 111, A07S11, doi:10.1029/2005JA011474, 2006.
- HERNÁNDEZ-PAJARES, M.; JUAN, J. M; SANZ, J; ARAGÓN-ÀNGEL, A. Propagation of medium scale traveling ionospheric disturbances at different latitudes and solar cycle conditions, **Radio Science**, v. 47, RS0K05, doi:10.1029/2011RS004951, 2012.
- HOFMANN-WELLENHOF, B.; LICHTENEGGER, H.; COLLINS, J; GPS - theory and practice. Wien: **Springer-Verlag**, 3 ed. 355 p. 1994.
- HUNSUCKER, R. D. Atmospheric gravity waves generated in the high latitude ionosphere: A review, **Rev. Geophys. Space Phys.**, v. 20, p. 293–315, 1982.
- JONAH, O. F.; KHERANI, E. A; DE PAULA, E. R. Observation of TEC perturbation associated with mediumscale traveling ionospheric disturbance and possible seeding mechanism of atmospheric gravity wave at a Brazilian sector, **Journal of Geophysical Research**, v. 121, doi:10.1002/2015JA022273, 2016.
- JONAH, O. F., KHERANI, E. A. AND DE PAULA E. R. Investigations of conjugate MSTIDS over the Brazilian sector during daytime, **J. Geophys. Res. S. Phys.**, 2017a, 122, doi:10.1002/ 2017JA024365.

- JONAH, O. F., COSTER, A., ZHANG, S., GONCHARENKO, L., ERICKSON, P. J., DE PAULA, E. R., & KHERANI, E. A. TID observations and source analysis during the 2017 Memorial Day weekend geomagnetic storm over North America. **J. of Geophys. Res.: S. Phys.**, 2018, 123. <https://doi.org/10.1029/2018JA025367>.
- KHERANI, E. A; LOGNONNÉ P; HÉBERT, H; ROLLAND, L; ASTAFYEVA, E; OCCHIPINTI, G; COISSON, P. WALWER, D; AND DE PAULA, E. R. Modelling of the total electronic content and magnetic field anomalies generated by the 2011 Tohoku-Oki tsunami and associated acoustic-gravity waves, **Geophysical Journal International**, v.191, p.1049–1066, doi: 10.1111/j.1365-246X.2012.05617.x, 2012.
- KHERANI, E. A. ROLLAND, L. LOGNONNÉ, P. SLADEN, A. KLAUSNER, V. DE PAULA, E. R. Traveling ionospheric disturbances propagating ahead of the Tohoku-Oki tsunami: A case study, **Geophysical Journal International**, vol. 204, p. 1148-1158, 2016.
- KELLEY, M. C. AND FUKAO, S. Turbulent upwelling of the mid- latitude ionosphere: 2. Theoretical framework, **Journal of Geophysical Research.**, 96, 37473753, 1991.
- KELLEY M.C. On the origin of mesoscale TIDs at midlatitudes, **Ann. Geophys.**, v. 29, p. 361–366, 2011, doi:10.5194/angeo-29-361, 2011.
- MEDVEDEV, A. S; YIGIT, E; HARTOGH, P; BECKER, E. Inuence of gravity waves on the Martian atmosphere: general circulation modeling, **Journal of Geophysical Research.**, 116, E10004, doi:10.1029/2011JE003848, 2011.
- NGWIRA, C. M., HABARULEMA, J. B. ASTAFYEVA, E. YIZENGAW, E. JONAH, O. F. CROWLEY, G. GISLER, A. AND COFFEY V., Dynamic response of ionospheric plasma density to the geomagnetic storm of 22-23 June 2015, **J. of Geophys. Res.**, S. Phys., 2019, <https://doi.org/10.1029/2018JA026172>.
- OTSUKA Y; SUZUKI, K; NAKAGAWA, S; NISHIOKA, M; SHIOKAWA, K; TSUGAWA, T. GPS observations of medium-scale traveling ionospheric disturbances over Europe **Ann. Geophys.**, v. 31, p. 163–172, 2013 doi:10.5194/angeo-31-163, 2013.
- OTSUKA, Y; SHIOKAWA, K; OGAWA, T; WILKINSON, P. Geomagnetic conjugate observations of medium-scale traveling ionospheric disturbances at midlatitude using all-sky airglow imagers, **Geophysical Research Letter**, 31, L15803, doi:10.1029/2004GL020262, 2004.

- PAVELIN, E; WHITEWAY, J.A; VAUGHAN, G. Observations of gravity wave generation and breaking in the lowermost stratosphere. **Journal of Geophysical Research**, v. 106: 2000JD9000480, 2001.
- PERKINS, F. Spread F and ionospheric currents, **Journal of Geophysical Research**, v. 78, p. 218–226, 1973.
- PFISTER, L; CHAN, K. R; BUI, T. P; BOWEN, S; LEGG, M; GARY, B; KELLY, K; PROFFITT, M; STARR, W. Gravity waves generated by a tropical cyclone during the STEP tropical field program: A case study, **Journal of Geophysical Research**, v. 98, p. 8611-8638, 1993.
- PIANI, C; DURRAN, D; ALEXANDER, M. J; HOLTON, J. R. A numerical Study of Three Dimensional Gravity Waves Triggered by Deep Tropical Convection and Their Role in the Dynamics of the QBO, **Journal of Atmospheric Science**, v. 57, p. 3689–3702, 2000.
- SHUME, E. B.; RODRIGUES, F. S.; MANNUCCI, A. J.; DE PAULA, E. R. Modulation of equatorial electrojet irregularities by atmospheric gravity waves. **Journal of Geophysical Research**, v. 119, p. 366–374, 2014. 66, 67, 74.
- TSUGAWA, T; SAITO, A; OTSUKA, Y; YAMAMOTO, M. Damping of large-scale traveling ionospheric disturbances detected with GPS networks during the geomagnetic storm, **Journal of Geophysical Research**, 108(A3), 1127, doi:10.1029/2002JA009433, 2004.
- TSUGAWA, T; OTSUKA, Y; COSTER, A. J; SAITO, A. Medium-scale traveling ionospheric disturbances detected with dense and wide TEC maps over North America, **Geophysical Research Letter**, 34, L22101, doi:10.1029/2007GL031663. 2007.
- VADAS, S. L. AND FRITTS, D. Influence of solar variability on gravity wave structure and dissipation in the thermosphere from tropospheric convection, **Journal of Geophysical Research**, 111, A10S12, doi:10.1029/2005JA011510, 2006.
- VADAS, S. L., J. AND LIU A. Generation of large-scale gravity waves and neutral winds in the thermosphere from the dissipation of convectively generated gravity waves, **Journal of Geophysical Research**, VOL. 114, A10310, doi:10.1029/2009JA014108, 2009
- VADAS, S. L; TAYLOR, M. J; PAUTET, P.D; STAMUS, P. A; FRITTS, D. C; LI, H.L ; SÃO SABBAS, F. T; RAMPINELLI, V. T; BATISTA, P; TAKAHASHI, H. Convection: The likely source of the medium-scale gravity waves observed in the OH airglow layer near Brasilia, Brazil, during the SpreadFEx campaign, **Ann. Geophys.**, v. 27, p. 231–259, doi:10.5194/angeo-27-231, 2009.

779 YIGIT, E; AYLWARD, A. D; MEDVEDEV, A. S. Parameterization of the effects of
780 vertically propagating gravity waves for thermosphere general circulation models:
781 Sensitivity study, **Journal of Geophysical Research**, v. 113, D19106,
782 doi:10.1029/2008JD010135, 2008.

783
784 YIGIT, E; MEDVEDEV, A. S; AYLWARD, A. D; RIDLEY, A. J; HARRIS, M. J;
785 MOLDWIN, M. B; HARTOGH, P. Dynamical effects of internal gravity waves in the
786 equinoctial thermosphere, **Journal of Atmospheric and Solar-Terrestrial**
787 **Physics**, v. 90-91, p. 104–116, doi:10.1016/j.jastp.2011.11.014, 2012.

788
789 ZETTERGREN, M. D., AND J. B. SNIVELY, Ionospheric response to infrasonic-
790 acoustic waves generated by natural hazard events, **Journal of Geophysical**
791 **Research**, 120, 8002–8024, doi:10.1002/2015JA021116, 2015.